

Effects of helium ion irradiation and thermal annealing on the optical and structural properties of hexagonal boron nitride

Guan-Lin Liu(刘冠麟), Ji-Lian Xu(徐辑廉), Peng-Tao Jing(景鹏涛), Jing-Jing Shao(邵京京), Xu Guo(郭旭), Yun-Tao Wu(吴韵涛), Feng Qin(覃凤), Zhen Cheng(程祯), Deming Liu(刘德明), Yang Bao(鲍洋), Hai Xu(徐海), Li-Gong Zhang(张立功), Da Zhan(詹达), Jia-Xu Yan(闫家旭), Lei Liu(刘雷), and De-Zhen Shen(申德振)
Citation: Chin. Phys. B, 2025, 34 (**5**): 057801. DOI: 10.1088/1674-1056/adbee7
http://cpb.iphy.ac.cn; http://iopscience.iop.org/cpb

What follows is a list of articles you may be interested in

Photoinduced Floquet higher-order Weyl semimetal in C_6 symmetric Dirac semimetals

Xin-Xin Xu(许欣欣), Zi-Ming Wang(王梓名), Dong-Hui Xu(许东辉), and Chui-Zhen Chen(陈垂针)
Chin. Phys. B, 2024, 33 (**6**): 067801. DOI: 10.1088/1674-1056/ad4634

Achieving high-performance multilayer $MoSe_2$ photodetectors by defect engineering

Jintao Hong(洪锦涛), Fengyuan Zhang(张丰源), Zheng Liu(刘峥), Jie Jiang(蒋杰), Zhangting Wu(吴章婷), Peng Zheng(郑鹏), Hui Zheng(郑辉), Liang Zheng(郑梁), Dexuan Huo(霍德璇), Zhenhua Ni(倪振华), and Yang Zhang(张阳)
Chin. Phys. B, 2021, 30 (**8**): 087801. DOI: 10.1088/1674-1056/abea8b

Faraday rotations, ellipticity, and circular dichroism in magneto-optical spectrum of moiré superlattices

J A Crosse and Pilkyung Moon
Chin. Phys. B, 2021, 30 (**7**): 077803. DOI: 10.1088/1674-1056/ac051f

Plasmonic properties of graphene on uniaxially anisotropic substrates

Shengchuan Wang(汪圣川), Bin You(游斌), Rui Zhang(张锐), Kui Han(韩奎), Xiaopeng Shen(沈晓鹏, and Weihua Wang(王伟华)
Chin. Phys. B, 2021, 30 (**3**): 037801. DOI: 10.1088/1674-1056/abd168

Extinction mechanisms of hyperbolic h-BN nanodisk

Runkun Chen(陈闰堃), Jianing Chen(陈佳宁)
Chin. Phys. B, 2020, 29 (**5**): 057802. DOI: 10.1088/1674-1056/ab8898

Effects of helium ion irradiation and thermal annealing on the optical and structural properties of hexagonal boron nitride

Guan-Lin Liu(刘冠麟)[1,2], Ji-Lian Xu(徐辑廉)[1], Peng-Tao Jing(景鹏涛)[1,†], Jing-Jing Shao(邵京京)[1,2], Xu Guo(郭旭)[1,2], Yun-Tao Wu(吴韵涛)[1,2], Feng Qin(覃凤)[1,2], Zhen Cheng(程祯)[1], Deming Liu(刘德明)[1], Yang Bao(鲍洋)[1], Hai Xu(徐海)[1], Li-Gong Zhang(张立功)[1], Da Zhan(詹达)[1], Jia-Xu Yan(闫家旭)[1], Lei Liu(刘雷)[1], and De-Zhen Shen(申德振)[1]

[1] *State Key Laboratory of Luminescence Science and Technology, Changchun Institute of Optics, Fine Mechanics and Physics, Chinese Academy of Sciences, Changchun* 130033, *China*

[2] *University of Chinese Academy of Sciences, Chinese Academy of Sciences, Beijing* 100049, *China*

(Received 22 January 2025; revised manuscript received 25 February 2025; accepted manuscript online 11 March 2025)

Hexagonal boron nitride (h-BN) has emerged as a promising two-dimensional material for quantum and optoelectronic applications, with its unique ability to host engineered defects enabling single-photon emission and spin manipulation. This study investigates defect formation in h-BN using focused helium ion beam (He^+ FIB) irradiation and post-annealing treatments. We demonstrate that helium ion irradiation at doses up to 2×10^9 ions/μm^2 does not induce phase transitions or amorphization. Spectroscopic analyses, including differential reflectance spectroscopy (DRS), photoluminescence (PL), and Raman spectroscopy, reveal substantial defect formation and structural modifications. Notably, the irradiation induces a softening of in-plane and interlayer phonon modes, characterized by frequency redshifts of 10.5 cm^{-1} and 3.2 cm^{-1}, respectively. While high-temperature thermal annealing mitigates lattice defects and facilitates single-photon emission, the E_{2g} peak width remains 38% broader and the shear mode peak width is 60% broader compared to pre-annealing conditions in the Raman spectra, indicating residual structural degradation. These findings provide insights into defect engineering mechanisms in h-BN, offering guidance for optimizing processing conditions and advancing quantum and optoelectronic device technologies.

Keywords: hexagonal boron nitride, focused ion beam, defect engineering, quantum materials, spectroscopy

PACS: 78.30.–j, 78.67.–n, 61.72.J–, 81.05.–t

DOI: 10.1088/1674-1056/adbee7 **CSTR:** 32038.14.CPB.adbee7

1. Introduction

Hexagonal boron nitride (h-BN) has attracted considerable attention in recent years as an emerging two-dimensional (2D) material with exceptional optical, electronic, and structural properties.[1–5] Its wide bandgap and robust lattice framework make h-BN uniquely suited for high-performance optoelectronic devices, while its 2D nature enables straightforward integration into existing semiconductor technologies.[3,4,6,7] An important feature of h-BN is its ability to host a variety of natural and engineered defects, some of which enable single-photon emission and others facilitate spin manipulation at room temperature — key phenomena for quantum information processing, secure communication, and nanoscale sensing.[5,7] The deterministic control of defect formation in h-BN addresses the challenge of random natural defects, enabling precise quantum device design.[8–10] Several advanced fabrication methods have been demonstrated for creating position-controlled defects in h-BN, including pre-fabricated nanopillar arrays,[11] AFM-based nanoimprinting,[12] femtosecond laser direct writing,[13,14] electron beam lithography,[15] and focused ion beam (FIB) processing.[16–22]

FIB has emerged as a versatile nanomanufacturing and micro-nanoscale analytical tool, enabling precise cutting, deposition, ion implantation, and surface modification. In the study of h-BN, high-energy ion beams can introduce highly precise defects ranging from color centers to spin defects.[16–22] Compared to Ga^+ or Xe^+ FIB, the helium ion microscope (HIM), also known as He^+ FIB, offers superior resolution, minimized lattice damage, and more precise defect control. These advantages enable the introduction of boron vacancies while preserving the crystal structure, thus facilitating high-quality quantum devices in h-BN.[23] Optimal He^+ FIB irradiation of h-BN generates V_B^- centers with enhanced PL, strong optically detected magnetic resonance (ODMR) contrast, and narrow spectral linewidths, improving magnetic sensing sensitivity and signal-to-noise performance.[18] Additionally, carefully regulated low-energy He^+ implantation allows for stable emission at 1.55 eV from 10 K to room temperature, verified by Raman and electron energy loss spectroscopies, providing a deterministic strategy for scalable quantum photonics.[20] In a further demonstration, position-controlled defect arrays in h-BN were created using He^+ FIB, with bright single-photon emitters achieved through oxygen annealing and parameter optimization, demonstrating < 50 nm

†Corresponding author. E-mail: jingpt@ciomp.ac.cn

© 2025 Chinese Physical Society and IOP Publishing Ltd. All rights, including for text and data mining, AI training, and similar technologies, are reserved.

localization precision.[19]

It should be noted that direct He^+ FIB processing typically generates V_B^- spin defects that require thermal annealing to become active single-photon sources.[18–20] A comprehensive characterization of the optical and vibrational properties of defect centers in h-BN is critical for elucidating their formation mechanisms. PL and Raman spectroscopy are commonly employed, alongside other non-destructive optical techniques such as differential reflectance spectroscopy (DRS)[24–26] and ultra-low-frequency Raman spectroscopy,[24,27–37] to investigate layer- and twist-angle-dependent properties in two-dimensional materials and the defect-induced changes in their optical characteristics. X. Hu *et al.* developed a DRS mapping-based method for quantifying defects, allowing high-throughput inspection of large areas of 2D materials like MoS_2 at the microscopic scale.[38] Meanwhile, P. Maguire *et al.* demonstrated that He^+ ion irradiation introduces lattice disorders in bilayer MoS_2, significantly affecting its low-frequency Raman spectra, with crystallite size and orientation identified as the main factors behind the observed redshift and shear-mode suppression.[35] In the case of layered h-BN, defects introduced by He^+ ion irradiation can be examined non-destructively via DRS and ultra-low-frequency Raman spectroscopy, offering important insights into irradiation-induced damage and defect behavior.

In this work, the evolution of defect formation in h-BN is investigated through an approach that combines focused helium ion beam irradiation with post-annealing treatments. A certain dose of helium ion irradiation does not induce phase transitions or amorphization in h-BN, but leads to defect-induced light absorption and photoluminescence. Raman spectroscopy reveals the softening of in-plane vibrational modes and interlayer shear mode phonons after helium ion beam irradiation. Following high-temperature thermal annealing, lattice defects are largely recovered, demonstrating activated single-photon emission; however, the broadening of the Raman peaks still indicates lower crystal quality, typically resulting from lattice defects, as well as the effects of stress and strain. These insights are pivotal for optimizing processing conditions and enhancing the performance of h-BN in future quantum and optoelectronic applications.

2. Results and discussion

2.1. Optical constrast and photoluminescence spectroscopy analysis of helium ion-irradiated h-BN

Figure 1(a) illustrates a schematic representation of the He^+ FIB irradiated h-BN sample. The HIM can achieve nanometer-scale imaging and processing with a resolution of up to 0.5 nm. The designated helium ion irradiation regions, marked by green boxes (see Fig. S1), correspond to ten different irradiation doses (1×10^7, 3×10^7, 5×10^7, 7×10^7, 9×10^7, 1×10^8, 3×10^8, 5×10^8, 1×10^9, and 2×10^9 ions/μm^2). Under conditions of an acceleration voltage of 30 kV and a beam current of 1 pA, the He^+ ions were irradiated perpendicularly onto the h-BN surface. Except for the irradiation area at a dose of 2×10^9 ions/μm^2, which was set to 2×2 μm^2, most other irradiation regions were configured to 3×3 μm^2. The high-energy He^+ ion beam induces sputtering of surface atoms and lattice damage in h-BN.[18,39–41] This study aims to elucidate these differences, providing insights into the defect dynamics of ion-irradiated h-BN.

Figure 1(b) presents the optical image of the h-BN sample following He^+ ions irradiation, along with fluorescent images under ultraviolet, blue, and green light channels. The thickness of the h-BN is approximately 46 nm, as confirmed by AFM measurements (see Fig. S2). Thicker h-BN layers (30–70 nm) were selected for their reduced fluorescence and improved stability, as thinner layers (<20 nm) are more susceptible to damage and high fluorescence. Subtle contrast differences between helium ion-irradiated and unirradiated regions can be observed in the optical image, attributed to the formation of color centers induced by He^+ ions irradiation. Fluorescence images further demonstrate that the introduction of defects significantly alters the optical properties of h-BN, including the absorption and emission characteristics of the color centers. This is further validated in Fig. 1(c), which presents the PL mapping image of the irradiated h-BN sample, showing that all irradiated regions exhibit PL emission. Representative PL spectra are shown in Figs. 1(d) and S3. Under lower-dose irradiation (5×10^7 ions/μm^2), the PL emission peak is located at 630 nm (1.97 eV), while under higher-dose irradiation (2×10^9 ions/μm^2), the PL emission peak redshifts to 660 nm (1.88 eV). To further investigate the absorption changes related to induced defects, Fig. 1(e) presents the representative DRS of the h-BN sample. The DRS characteristic peaks are observed at 614 nm (2.02 eV) and 625 nm (1.98 eV), corresponding to irradiation doses of 5×10^7 ions/μm^2 and 2×10^9 ions/μm^2, respectively. The complete DRS spectra for all irradiation doses are shown in Fig. S4. As shown in the inset of Fig. 1(e), the $\Delta R/R$ signals at 614 nm initially increase with irradiation dose, reaching a maximum at $\sim 5\times10^7$ ions/μm^2, before declining at higher doses. This non-monotonic trend arises from a combination of defect formation, lattice damage, and optical interference effects. The DRS peak position is also influenced by the thickness of the sample. In samples with thicknesses of 40–70 nm, the peaks predominantly appear in the 600–630 nm range, while thinner (~ 20 nm) and thicker (>90 nm) samples exhibit shifts toward ~ 550 nm and ~ 470 nm, respectively (see Fig. S5). These variations suggest that interference effects, in addition to defect-induced absorption, significantly shape the DRS spectra.

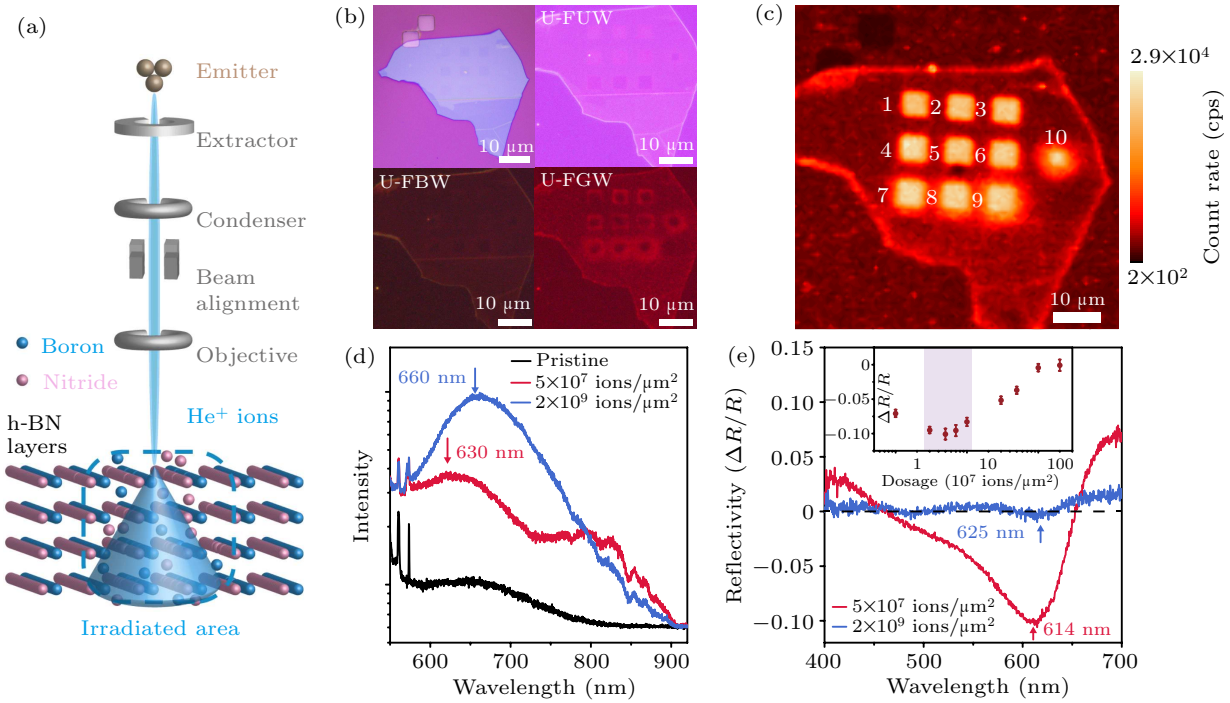


Fig. 1. (a) Schematic diagram of irradiation of h-BN sample with He^+ FIB. (b) Optical images of the h-BN sample, patterned via He^+ ion irradiation, captured under white light and fluorescence channels corresponding to ultraviolet (U-FUW), blue (U-FBW), and green (U-FGW) light. (c) PL emission mapping image of h-BN sample after irradiation of He^+ ions with different doses from 1×10^7 ions/μm^2 to 2×10^9 ions/μm^2. (d) Representative PL spectra of irradiation regions on h-BN sample. (e) Representative DRS spectra, with the inset showing the variation of the $\Delta R/R$ at 614 nm as a function of He^+ ion irradiation dose.

2.2. Raman spectroscopy analysis of helium ion-irradiated h-BN

Thus, further structural analysis is necessary to understand this phenomenon at varying irradiation doses. Raman spectroscopy, as an efficient, effective, and non-destructive structural characterization technique,[22,24,42–45] is used. Figure 2(a) illustrates the vibrational schematic of the E_{2g} Raman mode in h-BN. The E_{2g} mode in h-BN is a characteristic high-frequency vibrational mode associated with in-plane vibrations of boron and nitrogen atoms. In this mode, the B and N atoms vibrate in opposite directions within the same atomic layer of the hexagonal lattice. This mode reflects the structural integrity and periodicity of the in-plane lattice. Figure 2(b) displays the Raman spectrum of the h-BN sample highlighting the characteristic E_{2g} peak located at 1368.2 cm^{-1}, consistent with previous studies.[42,43,46,47] The E_{2g} peak shifts to lower wavenumbers and broadens significantly, reflecting the structural disorder introduced by defects formation. A new defect-related peak near 1295 cm^{-1} appears in irradiated regions, redshifts and intensifies with increasing helium ion dose, and correlates with the vibrational modes and rising density of irradiation-induced defects.[18,48] This observation aligns with prior research on the formation of V_B^- defects in h-BN through He^+ ions irradiation.[19,20]

To further validate this observation, the experiments were repeated using both 473 nm and 633 nm lasers, as shown in Fig. S6. The intensity of the E_{2g} Raman peak is relatively weak under 633 nm excitation because the Raman signal is inversely proportional to the fourth power of the wavelength ($I \propto 1/\lambda^4$).[49] The defect-related Raman peaks at 1295 cm^{-1} were not observed under 633 nm excitation. In the previous report, this defect-related Raman peak is absent under UV excitation (244 nm or 325 nm) and only observed under blue-green light excitation (488 nm, 514 nm, or 532 nm).[20] Combining our experimental results with previously reported findings, this defect-related Raman peak can only be observed under blue or green light excitation. Neither higher-energy UV light nor lower-energy red light excitation can detect this defect-related Raman peak, which may be associated with the energy level position of defects within the bandgap of h-BN. The localized vibrational modes induced by defects are attributed to the reduced crystal symmetry caused by He^+ ion irradiation, similar to observations in Ar^+-irradiated MoS_2.[50]

Figure 2(c) illustrates the relationship between the E_{2g} mode peak frequency (ω) and the full width at half maximum (FWHM or Γ) as a function of helium ion irradiation dose. The broadening of the E_{2g} peak, with its FWHM increasing from 8.3 cm^{-1} to 54.9 cm^{-1} and its peak position redshifting from 1368.2 cm^{-1} to 1357.7 cm^{-1}, reflects the increasing structural disorder caused by helium ion irradiation. The introduction of defects disrupts the lattice periodicity, which softens the phonon modes, leading to changes in both the peak frequency and FWHM. The experimentally measured frequencies and FWHM of the Raman mode can be fitted according

to the following empirical formulas:

$$\omega = \omega_0 + \alpha\sqrt{S}, \tag{1}$$

$$\Gamma = \Gamma_0 + \beta\sqrt{S}, \tag{2}$$

where ω and Γ represent the Raman vibration frequency and FWHM of the irradiated h-BN, while ω_0 and Γ_0 correspond to the Raman vibration frequency and FWHM of the untreated h-BN, respectively, S denotes the helium ion dose.[51] Here for the E_{2g} mode, the fitting parameters α and β for vibration frequency and FWHM are -2.43×10^{-4} and 1.08×10^{-3}, respectively. These equations reflect how defect accumulation modifies the vibrational properties of h-BN. As the irradiation dose increases, the introduction of vacancies and interstitial atoms locally disturbs the lattice, weakening its periodicity. This results in the softening of phonon modes, manifesting as a redshift in ω and an increase in Γ. The observed square root dependence on dose ($\sqrt{S}$) suggests that the defect-induced disorder follows a diffusion-like process, where the increase in defect density is not purely linear but rather follows a power-law behavior.

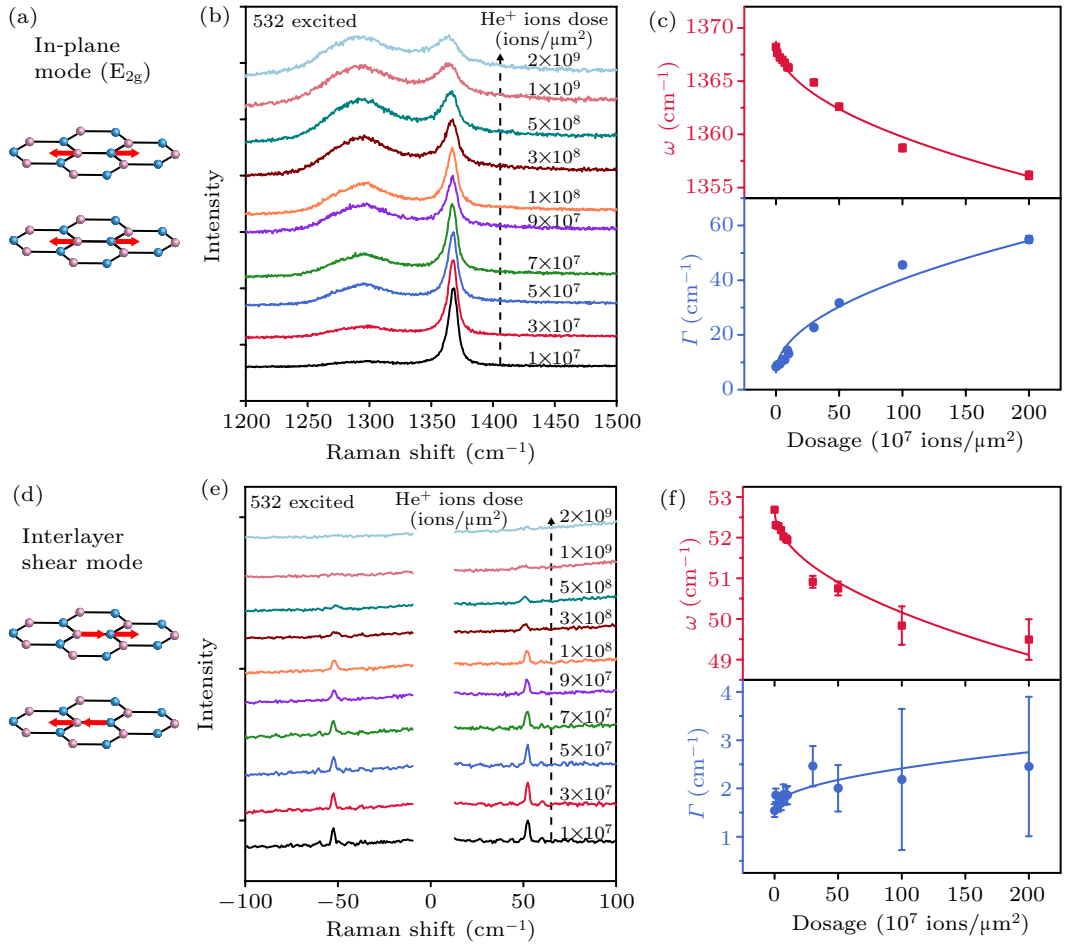


Fig. 2. (a) Schematic diagram of the E_{2g} vibrational mode. (b) Raman spectra ranging from 1200 cm^{-1} to 1500 cm^{-1} under 532 nm excitation. (c) Peak position and FWHM of the E_{2g} mode as a function of irradiation dose. (d) Schematic diagram of the interlayer shear vibrational mode. (e) Raman spectra ranging from -100 cm^{-1} to 100 cm^{-1} under 532 nm excitation for different irradiation doses. (f) Peak position and FWHM of the SM mode as a function of irradiation dose.

Beyond affecting the E_{2g} mode, the defects introduced by helium ion irradiation also influence interlayer coupling interactions. To explore these effects, ultra-low-frequency Raman measurements were conducted, extending down to frequencies as low as 10 cm^{-1}.[52] The shear mode in h-BN refers to a vibrational mode where adjacent atomic layers slide relative to each other in opposite directions, as shown in the schematic diagram of Fig. 2(d). The shear mode is sensitive to the interlayer coupling strength and the number of layers, making it useful for studying the structural and mechanical properties of h-BN.[28–30] The low-frequency Raman spectroscopy results are shown in Fig. 2(e), highlighting that the shear mode peak of unprocessed h-BN is located at 52.7 cm^{-1}. With increasing helium ion irradiation doses, the shear mode exhibits significant changes: the peak position redshifts from 52.7 cm^{-1} to 49.5 cm^{-1}, while its FWHM broadens from 1.5 cm^{-1} to 2.5 cm^{-1}, accompanied by a progressive decrease in peak intensity. Based on Eqs. (1) and (2), the shear mode fitting yields $\alpha = -7.99\times10^{-5}$ and $\beta = 2.57\times10^{-5}$, as illustrated in Fig. 2(f). The observed redshift of the shear mode peak indicates a weakening of interlayer coupling, due to defects introduced by helium ion irradiation, which disrupt the struc-

tural integrity of the coupling. Simultaneously, the broadening of the peak reflects a loss of periodicity in the h-BN layers, resulting in increased vibrational disorder. At high doses ($\geq 1\times10^9$ ions/μm^2), the shear mode signal is significantly weakened or even entirely suppressed, corresponding to extensive damage to the layered structure of h-BN.

The interlayer vibrational modes of h-BN can be described using the linear chain model (LCM). In this model, each rigid layer is represented as a sphere connected by van der Waals forces, assuming no relative atomic motion within the individual layers. For a 2D material consisting of N layers, the vibrational frequencies can be analytically expressed by the following equation:

$$\omega_{\mathrm{SM}} = \sqrt{\alpha^{\parallel}/\pi c^2 \mu}\,\sin\left(\mathrm{j}\pi/2N\right), \tag{3}$$

where $c = 3\times10^8$ m·s^{-1} is the speed of light, and μ is the mass per unit area of a single layer, for h-BN here $\mu = 6.9\times10^{-7}$ kg/m^2, $\alpha^{\parallel}$ is the nearest neighbor force constant of out-of-plane interlayer coupling.[53,54] The calculated data, including the interlayer coupling strength derived from the LCM model for hexagonal boron nitride after helium ion irradiation, are presented in Table S1. These results show that the interlayer coupling force in h-BN decreases from 1.7×10^{19} N/m^3 in the unirradiated state to 1.5×10^{19} N/m^3 at the highest irradiation dose, providing quantitative insights into the structural modifications induced by helium ion processing.

To verify whether He^+ ions irradiation induces phase transitions or amorphization in h-BN, selected area electron diffraction (SAED) and high-resolution transmission electron microscopy (HR-TEM) were employed, as shown in Figs. 3(a) and 3(b). Combined with SAED patterns, which exhibit sixfold symmetry, the HR-TEM analysis confirms the absence of significant amorphization or phase transitions in the irradiated h-BN material. The profiles along the two selected lines (red/blue) are shown in Fig. 3(c), revealing the periodicity of the crystal plane spacing. To the right of Fig. 3(c) is a schematic representation of the hexagonal boron nitride structure. By statistically analyzing the interplanar spacing of pristine and He^+ ions irradiated h-BN (Fig. 3(d)), the average interplanar distance is approximately 0.25 nm for both regions. While the irradiated region exhibited a slight increase in the dispersion of interplanar spacing, no significant amorphization or phase transformation was observed. These findings suggest that the structural integrity of the h-BN crystal lattice is largely maintained despite the ion irradiation, with damage primarily manifesting as localized point defects rather than widespread structural disruption.

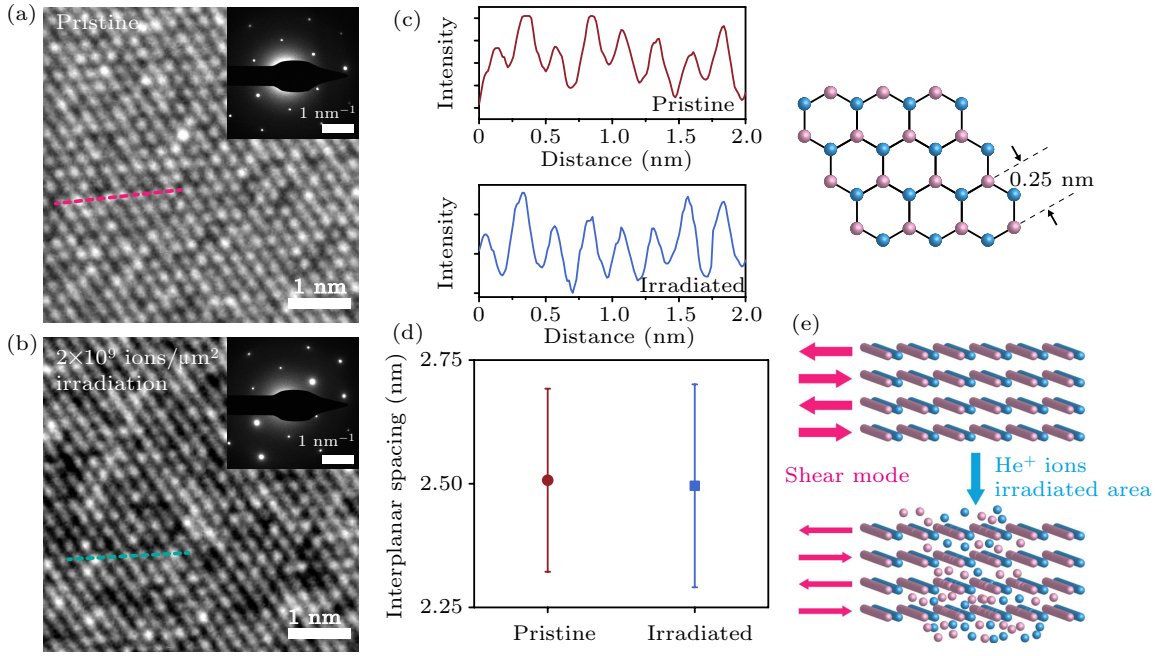


Fig. 3. The HR-TEM images and SEAD patterns (inset) of h-BN regions (a) without and (b) with irradiation of dose 2×10^9 ions/μm^2. (c) The profiles measured along the red and blue lines in (a) and (b), illustrating the interplanar spacing of h-BN. (d) The statistical results of interplanar spacing for He^+ ions irradiated and unirradiated regions of h-BN. (e) Schematic of interlayer coupling and structural changes in h-BN before and after He^+ ions irradiation.

Through a systematic characterization combining PL, DRS, Raman spectroscopy, TEM, and SAED, we provide a comprehensive analysis of the effects of helium ion irradiation on h-BN. With increasing irradiation dose, the defect density progressively rises, as reflected in the broadening and softening of the E_{2g} mode, shear mode SM, and the emergence of the defect-related Raman peak at 1295 cm^{-1}. The HR-TEM and SAED results confirm that these structural changes are dominated by point defects, such as vacancies and interstitial atoms, without evidence of amorphization or phase transitions. The

non-monotonic trends in DRS signals are possibly caused by the combined effects of defect accumulation, increased surface roughness, and localized lattice disruptions. These findings, combined with empirical fitting of vibrational frequencies and peak broadening as a function of irradiation dose, establish a quantitative framework to describe the structural evolution of h-BN under helium ion irradiation, as schematically illustrated in Fig. 3(e). The study explores the complex interplay between defect-induced structural changes and optical responses, offering insights into defect engineering for material optimization and technological applications.

2.3. Optical properties of helium ion-irradiated h-BN after annealing

Ion implantation and thermal annealing are critical processes in modern semiconductor manufacturing.[55] Previous studies have shown that while helium ion irradiation introduces initial defects, subsequent thermal annealing is essential to activate these defects and enable the formation of single-photon emitters in h-BN.[19] Motivated by this, we investigated the effects of annealing on the optical and vibrational properties of helium ion-irradiated h-BN. Figure 4(a) presents a comparison of the DRS spectra of h-BN irradiated with a dose of 5×10^7 ions/μm^2 before and after annealing, revealing a significant reduction in DRS intensity post-annealing. The inset shows the optical image of the sample post-annealing, where irradiated regions are now difficult to distinguish from the surrounding areas, consistent with the DRS results. The complete DRS results of annealed h-BN are shown in Fig. S7. After annealing, a single-photon emitter was observed in the region (denoted by the green dashed box in the third column of the first row) irradiated with a dose of 5×10^7 ions/μm^2. The corresponding spectrum (marked by a red circle within the green dashed box) is shown in Fig. 4(b), with the inset displaying its second-order correlation function, yielding a $g^2(0)$ value of 0.19, underscoring its distinct quantum emission characteristics. Similarly, the PL mapping results in the inset demonstrate that, after annealing, primarily regions irradiated with doses exceeding 5×10^8 ions/μm^2 exhibit significant PL signals above the background level, while lower-dose regions show PL signals nearly indistinguishable from those of untreated areas. Complete PL results of annealed h-BN are provided in Fig. S8. A systematic comparison of the

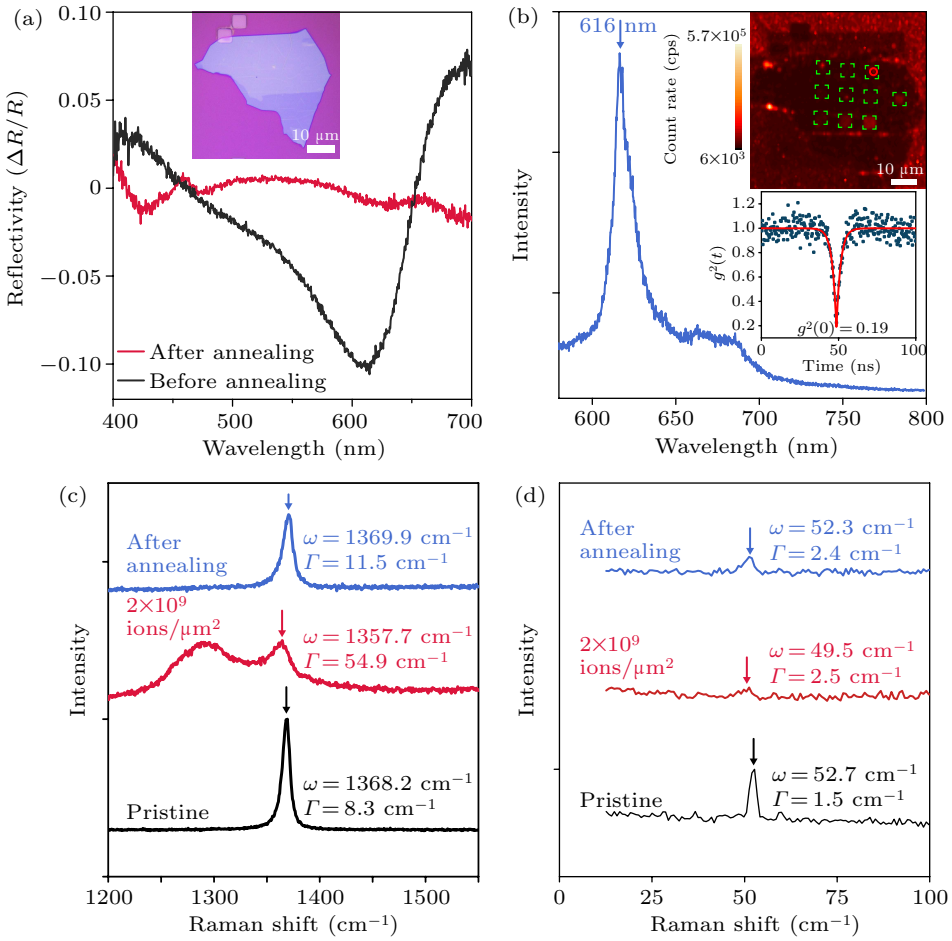


Fig. 4. (a) Comparison of DRS spectra for irradiated h-BN before and after annealing. The inset presents the optical image of the irradiated sample following annealing. (b) Spectrum of the single-photon emitter generated in the 5×10^7 ions/μm^2 region following annealing. The insets display the PL mapping (with a red circle marking the single-photon emitter) and the corresponding second-order correlation function measurement. Comparison of the (c) E_{2g} and (d) shear mode Raman spectra for the h-BN region with 2×10^9 ions/μm^2 before and after annealing, highlighting significant peak broadening, redshift, and recovery, along with the disappearance of the defect-related peak post-annealing.

PL spectra across ten different doses, before and after annealing, is presented in Fig. S9. The Raman spectra of h-BN irradiated with a dose of 2×10^9 ions/μm^2 before and after annealing, along with that of pristine h-BN, are shown in Figs. 4(c) and 4(d). The results demonstrate that the broadening and redshift of the E_{2g} mode induced by irradiation were effectively reversed after annealing, indicating the restoration of in-plane structural periodicity. The peak position shifted from 1357.7 cm^{-1} to 1369.9 cm^{-1}, and the FWHM decreased from 54.9 cm^{-1} to 11.5 cm^{-1}, further confirming the recovery of in-plane structural periodicity. After annealing, the formation of wrinkles in h-BN introduces tensile strain or compression, leading to slight shifts in the E_{2g} peak position compared to the untreated regions. Furthermore, the low-frequency Raman spectra reveal that the shear mode is only partially restored. Although the peak position shifts from 49.5 cm^{-1} to 52.3 cm^{-1} and the FWHM decreases slightly from 2.5 cm^{-1} to 2.4 cm^{-1}, it remains 60% broader than the 1.5 cm^{-1} FWHM of pristine (unirradiated) h-BN. This indicates that residual defects induced by high-dose irradiation continue to disrupt interlayer coupling. The Raman spectrum at the highest irradiation dose was selected for presentation because the structural damage is most severe at this dose, providing a clear demonstration of the effect of thermal annealing on defect recovery. The complete Raman results, including the peak positions and FWHMs of annealed h-BN under various helium ion irradiation doses, are provided in Fig. S10. Collectively, these results demonstrate the impact of annealing on repairing lattice defects and restoring optical and vibrational properties, contributing to the understanding of h-BN defect engineering. The framework established by integrating DRS, Raman, and PL characterizations also holds promise for application in online inspection and automated optical inspection, driving advancements in h-BN based quantum photonic technologies.

3. Conclusions

This study investigates the evolution of defect formation in h-BN through a combination of focused helium ion beam irradiation and subsequent post-annealing treatments. Our findings indicate that a certain dose ($\leq 2\times10^9$ ions/μm^2) of helium ion irradiation does not induce phase transitions or amorphization in h-BN. Helium ion irradiation induces substantial defect formation in h-BN, with the presence and characteristics of these defects substantiated through DRS and PL spectral measurements, revealing pronounced defect-mediated light absorption and photoluminescence. Raman spectroscopic analysis reveals a notable softening of in-plane vibrational mode and interlayer shear mode phonons following He^+ FIB irradiation, characterized by frequency redshifts of 10.5 cm^{-1} and 3.2 cm^{-1}, which suggests profound modifications in the material's structural integrity. Although high-temperature thermal annealing effectively mitigates lattice defects and facilitates activated single-photon emission, the observed broadening of Raman peaks, with 38% increase in E_{2g} peak width and 60% increase in shear mode peak width compared to the pristine h-BN, indicates that crystal quality remains partially degraded. This degradation is primarily attributed to the presence of residual lattice defects and the induced stress and strain within the material's structural framework. By elucidating the intricate mechanisms of defect formation and recovery in h-BN, these insights provide guidance for optimizing processing conditions and paving the way for advanced quantum and optoelectronic device applications.

Appendix A: Experimental details

A1. Sample fabrication and characterization

The h-BN samples, sourced from Shanghai Onway Technology Co., Ltd., were mechanically exfoliated onto pre-patterned SiO_2/Si substrates featuring a 300 nm SiO_2 layer with etched reference markers for precise localization. The preparation process involved cleaning the samples with UV-ozone treatment (Setcas, SC-UV-I) for 30 minutes to remove residual adhesive from the transfer tape. Following this, thermal annealing was conducted at 200 °C for 1 hour in an air atmosphere using a tube furnace to mitigate oxidation effects caused by ozone treatment. Helium ion irradiation was performed using a Zeiss Orion Nanofab system at 30 kV and 1 pA to introduce defects into the h-BN structure. For surface characterization, atomic force microscopy (AFM) measurements were carried out using a Park NX10 AFM. To analyze structural changes, h-BN samples were transferred onto carbon-supported copper grids, irradiated in square regions with a He^+ focused ion beam (FIB), and subsequently examined for lattice modifications using high-resolution transmission electron microscopy (HRTEM) and selected area electron diffraction (SAED) with a Thermo Fisher Scientific FEI Talos 200S.

A2. Optical measurements

The samples were analyzed using a home-built confocal optical microscope equipped for spectral measurements and anti-bunching testing. The excitation source was a 532 nm continuous-wave laser (Changchun New Industries Optoelectronics) directed onto the sample via a dichroic mirror and focused through a 100× objective lens with a numerical aperture (NA) of 0.9 (Olympus). Fluorescence signals, filtered using a long-pass filter, were collected into an optical fiber and transmitted to either an imaging spectrometer with a liquid nitrogen-cooled camera (Princeton Instruments, IsoPlane-320A and PyLoN 400B) or a Hanbury Brown and Twiss (HBT) setup equipped with two single-

photon avalanche diodes (SPADs) (Excelitas, SPCM-AQRH-14-TR). Time-correlated single-photon counting for anti-bunching measurements was performed using a PicoQuant MultiHarp 150 module.

Raman spectroscopy was carried out in a backscattering geometry using a Horiba HR550 Raman spectrometer coupled with a liquid nitrogen-cooled CCD detector (Horiba, Symphony SII-1LS-256-BD-PS). The excitation sources included a 633 nm He–Ne laser (Newport) and a 532 nm diode-pumped solid-state laser (Cobolt), with laser power maintained below 5 mW to minimize sample heating. To suppress unwanted signals, a BragGrate bandpass filter (OptiGrate, BPF) was employed to remove plasma lines, and Rayleigh scattering was eliminated using three BragGrate notch filters (OptiGrate, BNF) with a spectral bandwidth of $\sim 10\ \mathrm{cm}^{-1}$. Argon gas was flowed over the sample to prevent interference from air-based low-frequency Raman peaks. The Raman signal was collected using a 100× objective lens (NA = 0.9) and analyzed with a 500 nm blazed 1800 g/mm ruled grating, providing high spectral resolution for low-frequency Raman modes.

The DRS measurements were performed using a microscope (Olympus, BX53) coupled with a spectrophotometer (Princeton Instruments, SP2300i with a PyLoN 400 camera) and a halogen lamp (U-HGLA), enabling precise detection of reflected light intensity variations. Fluorescence imaging of the h-BN samples was conducted by exciting the samples with a mercury lamp (U-HGLS) and employing specific filter cubes (U-FUW, U-FBW, and U-FGW) integrated into the microscope. The images were captured using a DP27 camera for further analysis.

Acknowledgement

Project supported by the National Natural Science Foundation of China (Grant Nos. 11727902, 12074372, 12174385, 12334014, and 12304112).

References

[1] Aharonovich I, Englund D and Toth M 2016 *Nat. Photonics* **10** 631
[2] Caldwell J D, Aharonovich I, Cassabois G, Edgar J H, Gil B and Basov D N 2019 *Nature Reviews Materials* **4** 552
[3] Liu X and Hersam M C 2019 *Nature Reviews Materials* **4** 669
[4] Turunen M, Brotons-Gisbert M, Dai Y, Wang Y, Scerri E, Bonato C, Jöns K D, Sun Z and Gerardot B D 2022 *Nature Reviews Physics* **4** 219
[5] Aharonovich I, Tetienne J P and Toth M 2022 *Nano Lett.* **22** 9227
[6] Zhao X Y, Huang J H, Zhuo Z Y, Xue Y Z, Ding K, Dou X M, Liu J and Sun B Q 2020 *Chin. Phys. Lett.* **37** 044204
[7] Toth M and Aharonovich I 2019 *Annu. Rev. Phys. Chem.* **70** 123
[8] Wan N H, Lu T J, Chen K C, Walsh M P, Trusheim M E, De Santis L, Bersin E A, Harris I B, Mouradian S L, Christen I R, Bielejec E S and Englund D 2020 *Nature* **583** 226
[9] Kianinia M, Xu Z Q, Toth M and Aharonovich I 2022 *Appl. Phys. Rev.* **9** 011306
[10] Li C, Fröch J E, Nonahal M, Tran T N, Toth M, Kim S and Aharonovich I 2021 *ACS Photonics* **8** 2966
[11] Li C, Mendelson N, Ritika R, Chen Y, Xu Z Q, Toth M and Aharonovich I 2021 *Nano Lett.* **21** 3626
[12] Xu X, Martin Z O, Sychev D, Lagutchev A S, Chen Y P, Taniguchi T, Watanabe K, Shalaev V M and Boltasseva A 2021 *Nano Lett.* **21** 8182
[13] Wang X J, Fang H H, Li Z Z, Wang D and Sun H B 2024 *Light: Science & Applications* **13** 6
[14] Gan L, Zhang D, Zhang R, Zhang Q, Sun H, Li Y and Ning C Z 2022 *ACS Nano* **16** 14254
[15] Fournier C, Plaud A, Roux S, Pierret A, Rosticher M, Watanabe K, Taniguchi T, Buil S, Quélin X, Barjon J, Hermier J P and Delteil A 2021 *Nat. Commun.* **12** 3779
[16] Ziegler J, Klaiss R, Blaikie A, Miller D, Horowitz V R and Aleman B J 2019 *Nano Lett.* **19** 2121
[17] Glushkov E, Macha M, Räth E, Navikas V, Ronceray N, Cheon C Y, Ahmed A, Avsar A, Watanabe K, Taniguchi T, Shorubalko I, Kis A, Fantner G and Radenovic A 2022 *ACS Nano* **16** 3695
[18] Liang H, Chen Y, Yang C, Watanabe K, Taniguchi T, Eda G and Bettiol A A 2022 *Advanced Optical Materials* **11** 2201941
[19] Liu G L, Wu X Y, Jing P T, Cheng Z, Zhan D, Bao Y, Yan J X, Xu H, Zhang L G, Li B H, Liu K W, Liu L and Shen D Z 2023 *Advanced Optical Materials* **12** 2302083
[20] Sarkar S, Xu Y, Mathew S, Lal M, Chung J Y, Lee H Y, Watanabe K, Taniguchi T, Venkatesan T and Gradečak S 2023 *Nano Lett.* **24** 43
[21] Das S, Melendez A L, Kao I H, García-Monge J A, Russell D, Li J, Watanabe K, Taniguchi T, Edgar J H, Katoch J, Yang F, Hammel P C and Singh S 2024 *Phys. Rev. Lett.* **133** 166704
[22] Venturi G, Chiodini S, Melchioni N, Janzen E, Edgar J H, Ronning C and Ambrosio A 2024 *Laser & Photonics Reviews* **18** 2300973
[23] Hlawacek G and Gölzhäuser A 2016 *Helium Ion Microscopy* Springer International Publishing)
[24] Li X L, Han W P, Wu J B, Qiao X F, Zhang J and Tan P H 2017 *Advanced Functional Materials* **27** 1604468
[25] Krečmarová M, Andres-Penares D, Fekete L, Ashcheulov P, Molina-Sánchez A, Canet-Albiach R, Gregora I, Mortet V, Martínez-Pastor J P and Sánchez-Royo J F 2019 *Nanomaterials* **9** 1047
[26] Niu Y, Gonzalez-Abad S, Frisenda R, Marauhn P, Drüppel M, Gant P, Schmidt R, Taghavi N S, Barcons D, Molina-Mendoza A J, De Vasconcellos S M, Bratschitsch R, Perez De Lara D, Rohlfing M and Castellanos-Gomez A 2018 *Nanomaterials* **8** 725
[27] Nguyen M H, Lim S Y, Taniguchi T, Wantanabe K and Cheong H 2021 *2D Mater.* **8** 045004
[28] Schué L, Stenger I, Fossard F, Loiseau A and Barjon J 2016 *2D Mater.* **4** 015028
[29] Stenger I, Schué L, Boukhicha M, Berini B, Plaçais B, Loiseau A and Barjon J 2017 *2D Mater.* **4** 031003
[30] Wang W, Li Z, Marsden A J, Bissett M A and Young R J 2021 *2D Mater.* **8** 035058
[31] Zhang H, Horvat J and Lewis R A 2020 2020 45*th International Conference on Infrared, Millimeter and Terahertz Waves (IRMMW-THz) Buffalo*, NY, USA 1
[32] Liang L, Zhang J, Sumpter B G, Tan Q H, Tan P H and Meunier V 2017 *ACS Nano* **11** 11777
[33] Pizzi G, Milana S, Ferrari A C, Marzari N and Gibertini M 2021 *ACS Nano* **15** 12509
[34] Lin K Q, Holler J, Bauer J M, Parzefall P, Scheuck M, Peng B, Korn T, Bange S, Lupton J M and Schüller C 2021 *Advanced Materials* **33** 2008333
[35] Maguire P, Downing C, Jadwiszczak J, O'Brien M, Keane D, McManus J B, Duesberg G S, McEvoy V N N and Zhang H 2019 *J. Appl. Phys.* **125** 064305
[36] Lui C H, Ye Z, Keiser C, Xiao X and He R 2014 *Nano Lett.* **14** 4615
[37] Lui C H and Heinz T F 2013 *Phys. Rev. B* **87** 121404
[38] Hu X, Qiu C, Wang J and Liu D 2021 *Advanced Materials Interfaces* **9** 2101612
[39] Hlawacek G, Veligura V, van Gastel R and Poelsema B 2014 *J. Vacuum Sci. Technol. B* **32** 020801
[40] Lehtinen O, Dumur E, Kotakoski J, Krasheninnikov A, Nordlund K and Keinonen J 2011 *Nuclear Instruments and Methods in Physics Research Section B: Beam Interactions with Materials and Atoms* **269** 1327
[41] Kotakoski J, Jin C H, Lehtinen O, Suenaga K and Krasheninnikov A V 2010 *Phys. Rev. B* **82** 113404
[42] Zhou H, Zhu J, Liu Z, Yan Z, Fan X, Lin J, Wang G, Yan Q, Yu T, Ajayan P M and Tour J M 2014 *Nano Research* **7** 1232
[43] Cai Q, Scullion D, Falin A, Watanabe K, Taniguchi T, Chen Y, Santos E J G and Li L H 2017 *Nanoscale* **9** 3059

[44] Vuong T Q P, Liu S, Van der Lee A, Cuscó R, Artús L, Michel T, Valvin P, Edgar J H, Cassabois G and Gil B 2017 *Nat. Mater.* **17** 152
[45] Reich S, Ferrari A C, Arenal R, Loiseau A, Bello I and Robertson J 2005 *Phys. Rev. B* **71** 205201
[46] Tran T T, Bray K, Ford M J, Toth M and Aharonovich I 2016 *Nat. Nanotechnol.* **11** 37
[47] Orofeo C M, Suzuki S, Kageshima H and Hibino H 2013 *Nano Research* **6** 335
[48] Sarkar S, Xu Y, Mathew S, Lal M, Chung J Y, Lee H Y, Watanabe K, Taniguchi T, Venkatesan T and Gradečak S 2023 *Nano Lett.* **24** 43
[49] Long D A 1977 *Raman spectroscopy* (New York. McGraw-Hill)
[50] Bae S, Sugiyama N, Matsuo T, Raebiger H, Shudo K I and Ohno K 2017 *Phys. Rev. Appl.* **7** 024001
[51] Maguire P, Downing C, Jadwiszczak J, O'Brien M, Keane D, McManus J B, Duesberg G S, Nicolosi V, McEvoy N and Zhang H 2019 *J. Appl. Phys.* **125** 064305
[52] Wu H, Lin M L, Zhou Y, Zhang X and Tan P H 2023 *Anal. Chem.* **95** 10821
[53] Tan P, Han W, Zhao W, Wu Z, Chang K, Wang H, Wang Y, Bonini N, Marzari N and Pugno N 2012 *Nat. Mater.* **11** 294
[54] Zhang X, Han W, Wu J, Milana S, Lu Y, Li Q, Ferrari A and Tan P 2013 *Phys. Rev. B* **87** 115413
[55] Su X, Gao N, Chen M, Xu H T, Wei X and Di Z F 2019 *Chin. Phys. Lett.* **36** 068501